Experimental Thermal and Fluid Science 74 (2016) 368–381

Contents lists available at ScienceDirect

Experimental Thermal and Fluid Science

journal homepage: www.elsevier.com/locate/etfs

Interaction between free-surface aeration and total pressure on a stepped chute

Gangfu Zhang, Hubert Chanson *

The University of Queensland, School Civil Engineering, Brisbane, QLD 4072, Australia

ARTICLE INFO

Article history:
Received 21 September 2015
Received in revised form 10 December 2015
Accepted 12 December 2015
Available online 30 December 2015

Keywords:
Air bubble entrainment, Total pressure
Turbulence
Coupling
Physical modelling
Stepped spillways

ABSTRACT

Stepped chutes have been used as flood release facilities for several centuries. Key features are the intense free-surface aeration of both prototype and laboratory systems and the macro-roughness caused by the stepped cavities. Herein the air bubble entrainment and turbulence were investigated in a stepped spillway model, to characterise the interplay between air bubble entrainment and turbulence, and the complicated interactions between mainstream flow and cavity recirculation motion. New experiments were conducted in a large steep stepped chute ($\theta = 45°$, $h = 0.10$ m, $W = 0.985$ m). Detailed two-phase flow measurements were conducted for a range of discharges corresponding to Reynolds numbers between 2×10^5 and 9×10^5. The total pressure, air–water flow and turbulence properties were documented systematically in the mainstream and cavity flows. Energy calculations showed an overall energy dissipation of about 50% regardless of the discharge. Overall the data indicated that the bottom roughness (i.e. stepped profile) was a determining factor on the energy dissipation performance of the stepped structure, as well as on the longitudinal changes in air–water flow properties. Comparative results showed that the cavity aspect ratio, hence the slope, has a marked effect on the residual energy.

1. Introduction

Stepped spillways have been used as flood release facilities for several centuries [11]. In the past few decades, advances in construction materials and techniques led to a regained interest in stepped spillway design [1,20,10,12]. The steps contribute to some dissipation of the turbulent kinetic energy and reduce or eliminate the need for a downstream stilling structure [15]. Stepped spillway flows are characterised by strong turbulence and air entrainment (Fig. 1). Early physical studies were conducted by Horner [29], Sorensen [43], and Peyras et al. [36] with a focus on flow patterns and energy dissipation. Many studies focused on steep chute slopes typical of concrete gravity dams ([39,9,34,8]. More recent studies were conducted on physical models with moderate slopes typical of embankment structures [35,30,22,5,6,45,50].

A key feature of stepped chute flows is the intense free-surface aeration observed in both prototype and laboratory (Figs. 1 and 2). A number of laboratory studies investigated systematically the air–water flow properties at step edges [32,17,44,7,4]. A few studies measured the two-phase flow properties inside and above the step cavities [26,23]. The stepped cavities act as macro-roughness, with intense cavity recirculation. To date the findings hinted a strong interplay between air bubble entrainment and turbulence, and complicated interactions between mainstream flow and cavity recirculation motion, although no definite conclusion has been drawn in terms of stepped spillway design.

The goal of this contribution is to examine the air bubble entrainment and turbulence in a stepped spillway model. New experiments were conducted in a large steep chute ($\theta = 45°$) equipped with 12 flat impervious steps ($h = 0.10$ m, $W = 0.985$ m). Detailed two-phase flow measurements were conducted for a range of discharges corresponding to the transition and skimming flow regimes. The total pressure, air–water flow and turbulence properties in the mainstream and cavity flows were documented systematically. It is the aim of this work to quantify the interplay between air bubble entrainment, turbulence and energy dissipation.

2. Experimental facility and instrumentation

New experiments were conducted in a large-size stepped spillway model located at the University of Queensland (Figs. 2 and 3). The facility consisted of a 12.4 m long channel. Three pumps driven by adjustable frequency AC motors delivered a controlled discharge to a 5 m wide, 2.7 m wide and 1.7 m deep intake basin

* Corresponding author. Fax: +61 (7) 33 65 45 99.
E-mail address: h.chanson@uq.edu.au (H. Chanson).
URL: http://www.uq.edu.au/~e2hchans/ (H. Chanson).

http://dx.doi.org/10.1016/j.expthermflusci.2015.12.011
0894-1777/

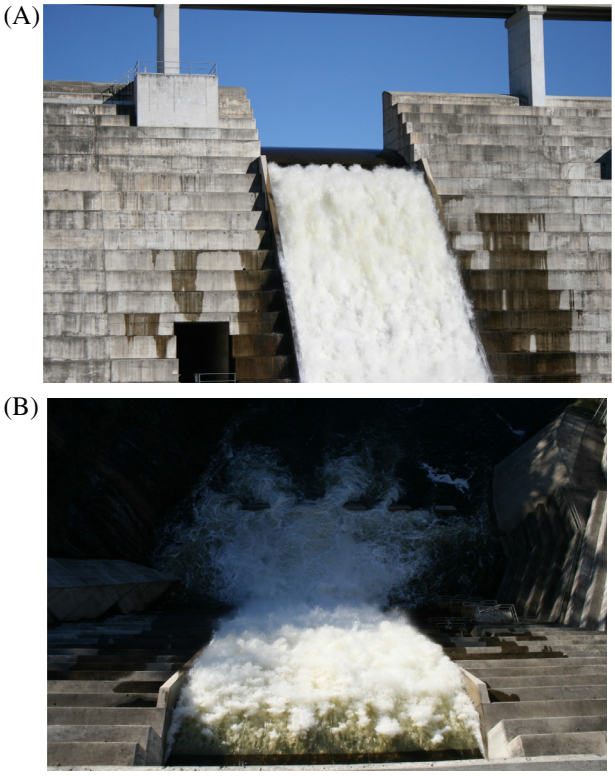

Fig. 1. Hinze dam stepped spillway in operation on 2 May 2015 ($\theta = 51.3°$, $h = 1.2$ m, $q = 2.15$ m^2/s, $Re = 8.5 \times 10^6$). (A) View from downstream and (B) view from the spillway crest.

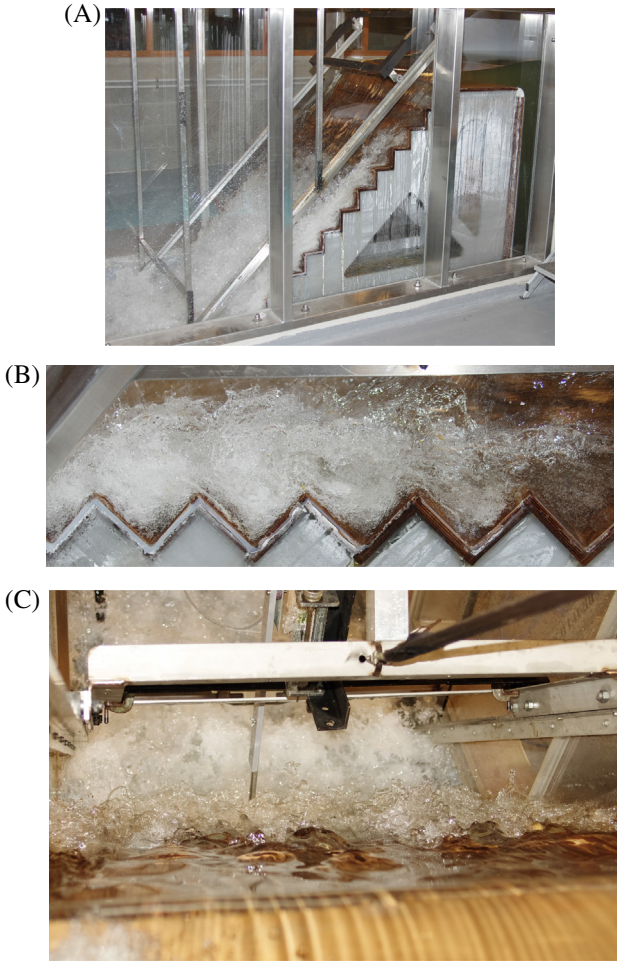

Fig. 2. Skimming flows above the stepped spillway model ($\theta = 45°$, $h = 0.1$ m, $l = 0.1$ m). (A) General view – flow conditions: $d_c/h = 1.08$, $Re = 4.4 \times 10^5$, (B) skimming flow above cavity recirculations, with flow direction from right to left – flow conditions: $d_c/h = 1.2$, $Re = 5.2 \times 10^5$ and (C) looking downstream at the upper spray region and splash structures, with the broad-crested weir overflow in foreground – flow conditions: $d_c/h = 1.5$, $Re = 7.2 \times 10^5$.

equipped with a carefully designed diffuser, followed by two rows of flow straighteners. The intake basin was connected to the test section through to a 2.8 m long 5.08:1 sidewall contraction. The entire setup resulted in a smooth and waveless inflow for discharges up to 0.30 m^3/s. The stepped chute was controlled by a broad-crested weir at the upstream end (Fig. 2A). The broad crest was horizontal, 0.6 m long and 0.985 m wide with a vertical upstream wall and an upstream rounded nose (0.058 m radius). During initial tests, the weir ended with a sharp edge (see below). Later a downstream rounded edge (0.018 m radius) was installed and all experiments were conducted with the downstream edge rounding. The stepped chute consisted of twelve 0.1 m high and 0.1 m long smooth flat steps made of plywood (Fig. 2). Each step was 0.985 m wide. The stepped chute was followed by a horizontal tailrace flume ending into a free overfall.

The discharge was deduced from detailed velocity and pressure measurements above the broad crested weir using a Dwyer® 166 Series Prandtl–Pitot tube connected to an inclined manometer, giving total head and piezometric head data [52]. The results yielded the following relationship between the discharge per unit width q and the upstream head above crest H_1:

$$q = \left(0.897 + 0.243 \times \frac{H_1}{L_{crest}}\right) \times \sqrt{g \times \left(\frac{2}{3} \times H_1\right)^3} \quad (1)$$

where g is the gravity constant and L_{crest} is the crest length ($L_{crest} = 0.60$ m) (Fig. 3). Clear-water flow depths were measured with a pointer-gauge on the channel centreline as well as dSLR photography (Canon™ 400D) through the sidewalls.

The air–water flow measurements were conducted using a dual-tip phase detection probe developed at the University of Queensland. The probe was capable of recording rapidly varying air–water interfaces based upon changes in resistivity and consisted of two identical tips, with an inner diameter of 0.25 mm, separated longitudinally by a distance Δx. The longitudinal separation Δx for each probe was 4.89 mm, 6.50 mm, 8.0 mm, and 8.42 mm. The probe sensors were excited by an electronic system and the signal output was recorded at 20 kHz per sensor for 45 s, following previous sensitivity analyses [47,25].

The instantaneous total pressure was measured with a MeasureX MRV21 miniature pressure transducer, its sensor featuring a silicon diaphragm with minimal static and thermal errors. The transducer was custom designed and measured relative pressures between 0 and 0.15 bars with a precision of 0.5% full scale. The signal was amplified and low-pass filtered at a cut off frequency of 2 kHz. The total pressure sensor was mounted alongside the dual-tip conductivity probe to record simultaneously the instantaneous total pressure and void fraction. The probes were sampled at 5 kHz per sensor for 180 s, following Wang et al. [49]. The data were sampled above each step edge downstream of the inception point of free-surface aeration.

A trolley system used to position the probes was fixed by steel rails parallel to the pseudo-bottom between step edges. The vertical movement of the probes was controlled by a Mitutoyo™ digital ruler within ±0.01 mm and the error on the horizontal position was less than 1 mm.

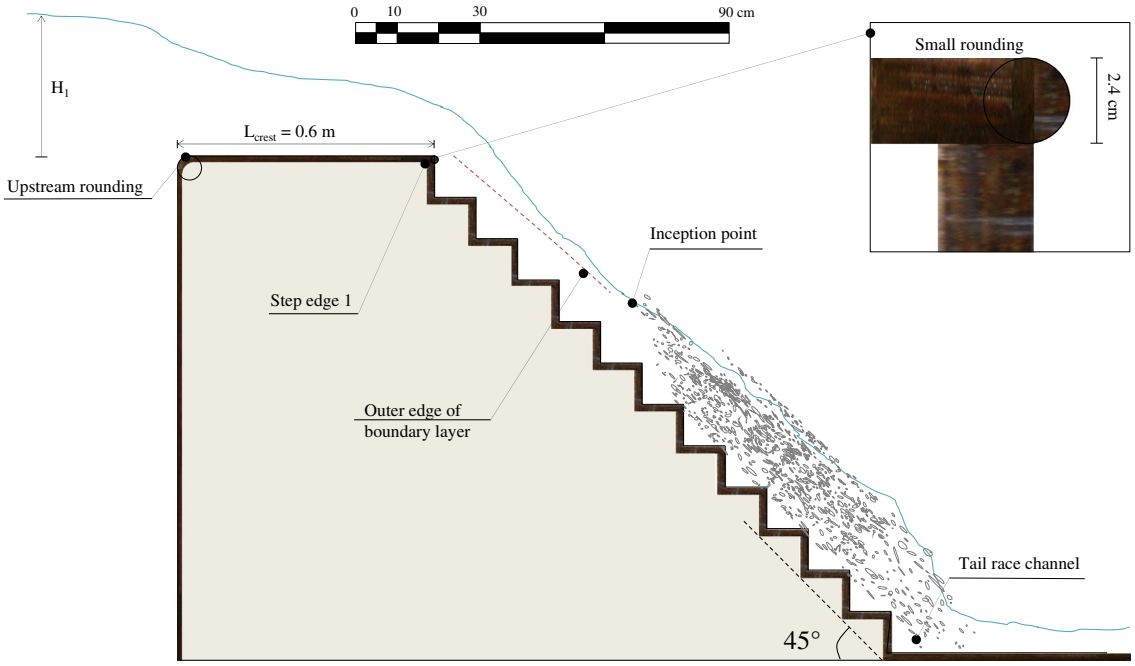

Fig. 3. Definition sketch of stepped spillway model.

2.1. Preliminary tests

Initial tests were conducted with a sharp downstream crest edge. Un-ventilated deflected jets were observed for $0.15 < H_1/L_{crest} < 0.44$. The results were quantitatively comparable to the findings of Pfister [37]. There were however some distinctive difference across the range of flow conditions, the worst deflecting jet conditions being observed for $0.18 < H_1/L_{crest} < 0.27$. For these conditions, deflecting jets took off at step edges 1 and 4, while large air cavities formed between step edges 1–3 and between step edges 4–6 respectively. Further a series of tests were performed systematically with a monotonically increasing discharge, followed by a monotonically decreasing flow rate. The results showed some marked hysteresis. The above quantitative observations were obtained with increasing discharges.

Following these initial tests, a 0.018 m radius rounded edge was installed at the downstream end of the broad crest (Fig. 3) and no further jet deflection was observed within $0.045 < d_c/h < 2$ where d_c is the critical flow depth ($d_c = (q^2/g)^{1/3}$) and h is the vertical step height ($h = 0.10$ m).

2.2. Experimental flow conditions

Total pressure and two-phase flow measurements were performed for a range of discharges encompassing transition and skimming flows, although the focus of the study was on the skimming flow regime. Two-phase flow measurements were undertaken at step edges in the aerated flow region for both transition and skimming flows. Next the measurements were repeated in and above several step cavities for a subset of skimming flow discharges. Lastly, simultaneous two-phase flow and total pressure measurements were conducted in the aerated flow region for a range of skimming flow conditions. The experimental flow conditions are summarised in Table 1.

3. Results (1) flow patterns

Visual observations were conducted for a broad range of dimensionless discharges d_c/h (Table 1). Three main flow regimes were identified, namely a nappe flow, a transition flow or a skimming flow regime depending upon the discharge. For $d_c/h < 0.15$, the water cascaded from one step to the next one and appeared highly fragmented. For $0.15 \leqslant d_c/h < 0.4$, a clear water supercritical jet developed downstream of step edge 2 and reattached upstream of step edge 5. The jet was deflected again off step 5 edge and a large amount of air was entrained. A transition flow was observed for $0.4 \leqslant d_c/h < 0.9$. For $0.4 \leqslant d_c/h < 0.6$, the step cavities downstream of the large clear water jet impact were partially filled and the flow appeared highly chaotic with strong splashing and spray. The upstream clear jet disappeared for $0.6 \leqslant d_c/h < 0.9$ where all cavities became partially filled with alternating cavity sizes, similar to previous observations (e.g. [18]. For $d_c/h \geqslant 0.9$, a skimming flow was observed (Fig. 2). The mainstream flow skimmed over the pseudo-bottom formed by the step edges as sketched in Fig. 3. The streamlines were approximately parallel, although the free-surface exhibited a wavy profile approximately in phase with the steps at lower discharges. At the upstream end, the flow was smooth and glassy. Downstream of the inception point of free-surface aeration, some complex air–water interactions were observed (Fig. 2). The flow in each step cavity exhibited a quasi-stable recirculation motion (Fig. 2B). Visual observations suggested strong mainstream–cavity flow interactions, as previously reported [39,17,26,4].

In the following sections, the focus will be on the transition and skimming flow regime, the latter being typical of steep stepped spillway operating at large flows during major floods [15].

4. Results (2) air–water flow properties at step edges

Detailed void fraction measurements were conducted with a dual-tip phase detection probe at all step edges downstream of the inception point. Typical void fraction distributions are presented in Fig. 4A and B for transition and skimming flows. For most flow rates, the results showed an S-shape typically observed on stepped spillways with flat steps [40,8,17]. The void fraction data showed some self-similarity except at the first step edge downstream of the onset of aeration. In the overflow above the stepped

Table 1
Experimental flow conditions.

Study type	Q (m^3/s)	d_c/h	Re	Locations	Flow regime	Remarks
Visual observations	0.001–0.24	0.045–1.8	4×10^4–9.7×10^5	Step edges 1–12	Nappe, transition, skimming	Clear water flow and aerated flow
Air–water flow measurements	0.057–0.216	0.7–1.7	2.3×10^5–8.7×10^5	Step edges 5–12	Transition, skimming	Aerated flow
	0.083–0.179	0.9–1.5	3.3×10^5–8.5×10^5	Step cavities 7–9 & 11–12	Skimming	Aerated flow
Total pressure & air–water measurements	0.083–0.216	0.9–1.7	3.3×10^5–8.7×10^5	Step edges 5–12	Skimming	Aerated flow

Notes: Q: water discharge; Re: Reynolds number defined in terms of hydraulic diameter.

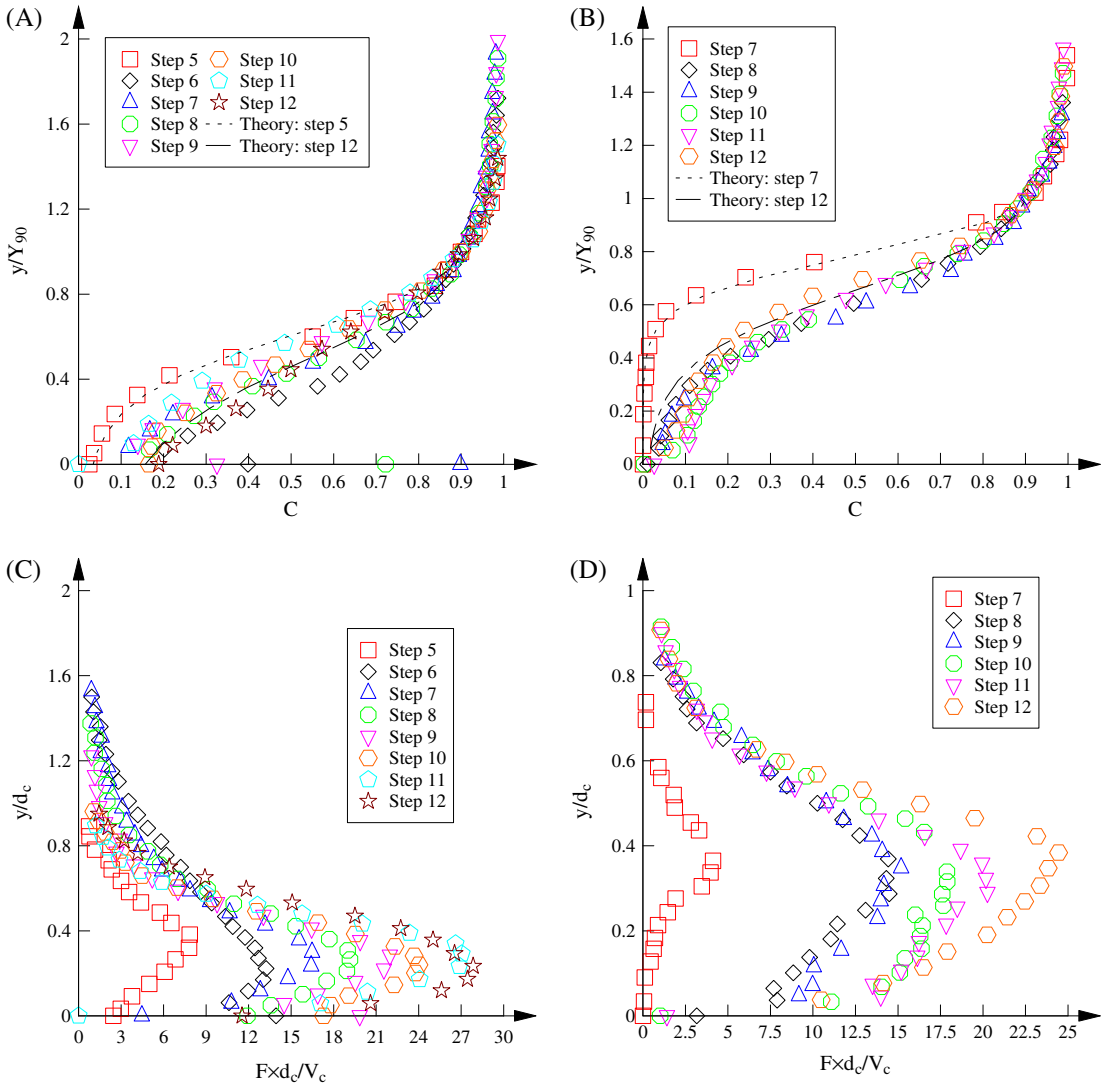

Fig. 4. Void fraction and bubble count rate distributions in the air–water flow region – geometry: $\theta = 45°$, $h = 0.10$ m. (A) Void fraction, $d_c/h = 0.7$, transition flow, (B) void fraction, $d_c/h = 1.3$, skimming flow, (C) bubble count rate, $d_c/h = 0.7$, transition flow and (D) bubble count rate, $d_c/h = 1.3$, skimming flow.

bottom, the void fraction data followed closely a theoretical distribution [17]:

$$C = 1 - \tanh^2\left[K' - \frac{y'}{2 \times D_0} + \frac{\left(y' - \frac{1}{3}\right)^3}{3 \times D_0}\right] \quad (2)$$

where $y' = y/Y_{90}$, y is the distance normal to the pseudo-bottom formed by the step edges, Y_{90} is the normal distance from the pseudo-bottom for $C = 0.9$, and K' and D_0 are functions of the depth-averaged void fraction C_{mean}:

$$C_{mean} = \frac{1}{Y_{90}} \times \int_0^{Y_{90}} C \times dy \quad (3)$$

Eq. (2) is plotted in Fig. 4 for the first and last step edges downstream of the inception point. Overall a good agreement was obtained, despite small scatter underlying void fraction and height measurements uncertainties.

The bubble count rate F is defined as half the number of air–water interfaces detected by the probe sensor per unit time. The bubble count rate is a function of the flow fragmentation. For a

given interfacial velocity, F is proportional to the specific interface area [13], thus providing some information on the re-aeration rate. Typical dimensionless bubble count rate $F \times d_c/V_c$ distributions are shown in Fig. 4C and D. The data showed a distinct shape, with a maximum bubble count rate F_{max} at about $0.3 < y/d_c < 0.4$ corresponding to a void fraction between 0.4 and 0.5, as previously reported [48,4].

The interfacial velocities were calculated based upon a cross-correlation method. The velocity data exhibited some self-similarity and they were approximately by a simple power law for $y < Y_{90}$ and an uniform profile above:

$$\frac{V}{V_{90}} = \left(\frac{y}{Y_{90}}\right)^{1/N} \qquad 0 < y < Y_{90} \tag{4a}$$

$$\frac{V}{V_{90}} = 1 \qquad y/Y_{90} \geqslant 1 \tag{4b}$$

where the interfacial velocity V was normalised in terms of the characteristic velocity V_{90} defined as the interfacial velocity for $C = 0.9$. The above relationships were compared successfully to data (data not shown), with a satisfactory agreement for $N = 10$ on average. For a given discharge, the velocity power law exponent N was observed to vary from one step to the next one, as shown by Felder and Chanson [22]. For a given discharge, the velocity power N showed some longitudinal fluctuation with a wavelength about 1–2 cavity lengths. Such a longitudinal variation in N was likely linked to the flow response to contraction and expansion, and interactions with vortices shed from the bottom roughness. Herein the longitudinal distribution of the velocity power N in skimming flows is plotted in Fig. 5, where x is the streamwise distance from step edge 1, x_i is the streamwise location of the inception point of free-surface aeration and L_{cav} is the cavity length ($L_{cav} = (h^2 + l^2)^{1/2}$). The data showed large scatter without correlation to the discharge.

The interfacial turbulence intensity is defined as the ratio of the root-mean-square of interfacial velocity fluctuations to the mean interfacial velocity: $Tu = \sqrt{\overline{v^2}}/V$. It was calculated based upon a cross-correlation technique between the probe signals [17]. Typical distributions are presented in Fig. 6. In the transition flow, the turbulence intensity data generally increased with increasing elevation, with local maxima next to the step edge at $y/d_c \approx 0.4$, which were respectively linked to the existence of a large number of air–water interfaces and irregular flow impingement on the horizontal step face [24]. In skimming flows, the data followed a characteristic shape with maximum turbulence levels at $y/d_c \approx 0.4$ (Fig. 6). Overall the turbulence levels tended to be larger in skimming flows than in transition flows. For all discharges, the local maxima in turbulence levels approximately occurred at those of maximum bubble count rates (see discussion below).

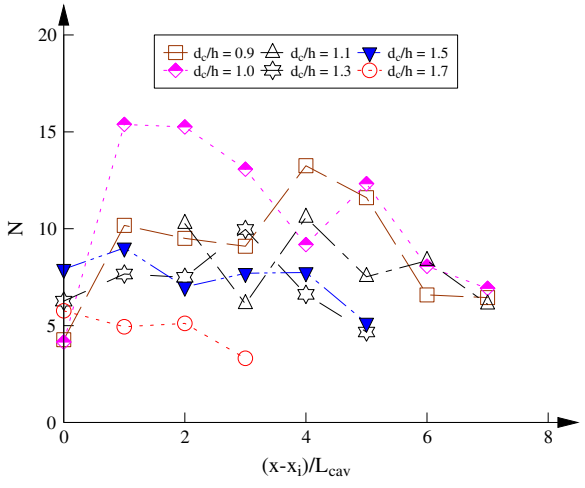

Fig. 5. Longitudinal variation of the velocity power law exponent N.

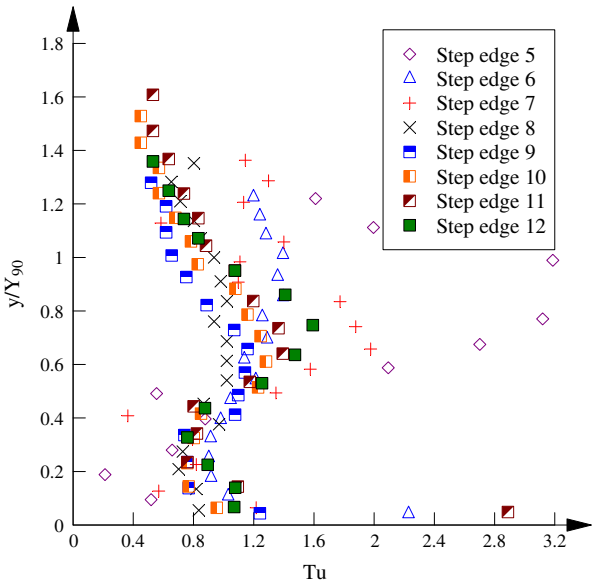

Fig. 6. Turbulence intensity distributions in air–water skimming flow – flow conditions: $\theta = 45°$, $h = 0.10$ m, $d_c/h = 0.9$, $Re = 3.3 \times 10^5$, interfacial turbulence intensity.

5. Results (3) total pressure measurements in the air–water flow region

Total pressure measurements were undertaken in the aerated flow region downstream of the inception point. The sensor was aligned with the main flow direction and recorded the instantaneous total pressure. Neglecting the surface tension effects during interfacial interactions with the probe sensor, the time-averaged total pressure at an elevation y equals:

$$P_t = \frac{1}{2} \times (1 - C) \times \rho_w \times (V_x^2 + \overline{v_x^2}) + \rho_w \times g \times \cos\theta \times \int_y^{Y_{90}} (1 - C) \times dy \tag{5}$$

where ρ_w is the water density, V_x is the time-averaged velocity of the water phase, $\overline{v_x^2}$ is the variance of the water velocity and θ is the angle between the pseudo-bottom and the horizontal. Eq. (5) assumes implicitly that the pressure distribution is hydrostatic taking into account the time-averaged void fraction distribution in the direction normal to the pseudo-bottom. Herein total pressure sensor measurements were compared to estimates derived from Eq. (5). Typical results are shown in Fig. 7, where the pressure sensor data P_t are compared to Eq. (5) (Fig. 7, black symbols). The total pressure sensor data showed a maximum corresponding to about $C = 0.5$. A reasonable agreement was observed between the measured and estimated total pressures (Eq. (5)) as illustrated in Fig. 7. The result implied that the hydrostatic pressure distribution assumption, taking into account the void fraction distribution and chute slope, might be a reasonable approximation in the aerated skimming flows.

Fig. 8A shows typical distributions of the root-mean-square of the total pressure fluctuations $\sqrt{\overline{p_t'^2}}$. The data presented a marked maximum about $y/Y_{90} = 0.7$, close to the location of maximum

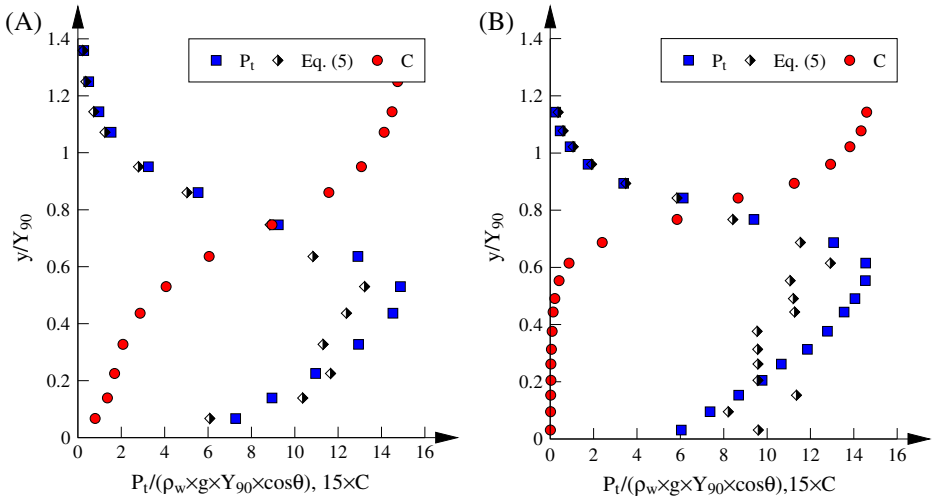

Fig. 7. Distributions of total pressure and void fraction in air–water skimming flows –comparison between total pressure sensor and Eq. (5). (A) d_c/h = 0.9, step edge 12 and (B) d_c/h = 1.7, step edge 9 (inception point).

bubble count rate F_{max}. Fig. 8B shows a typical relationship between the bubble count rate F and the total pressure fluctuations in skimming flow. In Fig. 8B, the data are normalised in terms of their respective maximum values at the corresponding cross sections: i.e., F/F_{max} and $\sqrt{\overline{p_t'^2}}/\sqrt{\overline{p_t'^2}}_{max}$. Overall the data indicated a strong positive correlation between the variables, indicating that the total pressure fluctuations were influenced by density fluctuations induced by strong turbulent diffusive actions. Note that the data also showed some hysteresis about F/F_{max} = 1. This might be linked to the roughness contributions to the total pressure fluctuations, which was significant next to the pseudo-bottom but decreased towards the upper free-surface.

The turbulence intensity in the water phase may be deduced from the total pressure fluctuations and void fraction with the approximate form:

$$Tu_p = \sqrt{\frac{\frac{\overline{p_t'^2}}{\rho_w^2 \times V_x^4} - \frac{1}{4} \times C \times (1-C)}{(1+\frac{1}{2}C) \times (1-C)}} \quad (6)$$

Fig. 9 presents the turbulent intensity distributions deduced from the total pressure sensor for the same flow conditions, as the data shown in Fig. 6. The results were obtained by applying Eq. (6), using void fraction measured with the phase-detection probe located 6.5 mm beside the total pressure probe sensor. The turbulent intensity in the water phase Tu_p was between 0.1 and 0.5 for all the discharges and locations along the chute. The data showed a local minimum about $(Tu_p)_{min} \approx 0.1 - 0.15$ about y/Y_{90} = 0.5 – 0.7. The total pressure sensor data (Fig. 9) may be compared to the interfacial turbulent intensities Tu deduced from a dual-tip conductivity probe (Fig. 6). The interfacial turbulent intensities were consistently larger in magnitude, ranging between 0.4 and 3.0. They also presented a different trend, with a local maximum about y/Y_{90} = 0.5 – 0.7. It is suggested that the velocity fluctuations of water particles were damped by the presence of a large number of air bubbles.

6. Results (4) air–water flow properties between step edges

Detailed air–water measurements were conducted at several locations between step edges for $0.9 \leqslant d_c/h \leqslant 1.5$, with the phase-detection probe aligned both parallel to the pseudo-bottom as well as in the direction perpendicular to the horizontal step face in the step cavities.

In the mainstream flow above step cavities, all void fraction data showed the same S-shape (Eq. (2)) for $y/Y_{90} > 0.3$. Typical data are shown in Fig. 10. Fig. 10B presents the longitudinal variation of void fraction along the pseudo-bottom (y = 0). The data showed a monotonic increase up to x_s/L_{cav} = 0.7, where x_s is the streamwise distance from the step edge: $x_s = x - x_i$. The presence of the cavity was felt on the void fraction in a region immediately above the pseudo-bottom (i.e. $y/Y_{90} < 0.3$). Fig. 10C shows a typical void fraction contour between step edges 7–9; the contour plot was constructed from discrete data samples recorded at locations marked by black dots. Overall the data indicated a lesser aeration in the step cavities compared to the mainstream flow above (Fig. 10C). A greater amount of air was trapped at the centre of the cavity than next to the step faces, as confirmed by visual observations. For all data, the void fraction distributions showed a local peak in the step cavities at $x_s/L_{cav} \approx 0.7$, comparable to previous data [23].

Bubble count rate measurements in the overflow above step cavities followed a distinctive shape, with maxima recorded at $y/d_c \approx 0.3 - 0.4$ corresponding to $C \approx 0.4 - 0.5$, as previously reported [17,26,23]. All data showed some scatter towards the pseudo-bottom because of cavity effects (data not shown). In the step cavities, the bubble rate distributions highlighted some effect of the developing shear layer downstream of each step edge, while an increase in bubble count rate was observed above each step edge because of the step-wake interactions. In the downstream cavity, lower bubble count rates were recorded because of flow expansion.

The interfacial velocity distributions presented some self-similarity. In the main stream, the data followed closely a power law (Eq. (4a)), with the best correlation for N = 8.5 (R = 0.84) in contrast to N = 10 observed at step edges. The difference might be related to a downward shift of the velocity profiles above the step cavity because of flow expansion. Typical velocity contours between step edges are shown in Fig. 11A and B for two skimming flow conditions. The flow was significantly faster at step edges than above step cavities, showing patterns consistent with flow expansion and contraction above each step cavity. The velocity contours highlighted a developing shear layer in the wake of each step edge. In Fig. 11C, the velocity distributions in the shear layer are compared to Tollmien and Goertler solutions for the plane shear layer [38,41]:

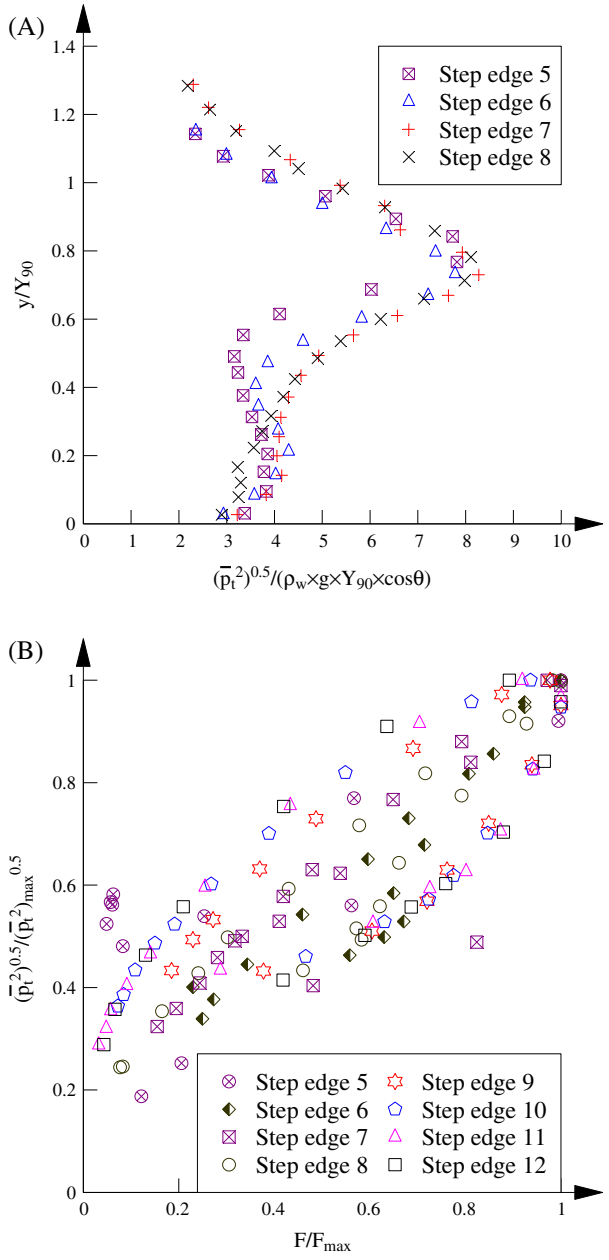

Fig. 8. Dimensionless distributions of total pressure fluctuations in the air–water flow region in skimming flows. (A) Distributions of total pressure fluctuations – flow conditions: $d_c/h = 1.7$, $Re = 8.7 \times 10^5$ and (B) relationship between dimensionless bubble count rate and total pressure fluctuations – flow conditions: $d_c/h = 0.9$, $Re = 3.3 \times 10^5$.

$$\frac{V}{V_0} = \frac{d}{d\varphi}\left[C_2 \times e^{-\varphi} + C_3 \times e^{\varphi/2} \times \cos\left(\frac{\sqrt{3}}{2} \times \varphi\right) + C_4 \times e^{\varphi/2} \times \sin\left(\frac{\sqrt{3}}{2} \times \varphi\right)\right] \quad \text{Tollmien solution} \tag{7}$$

$$\frac{V}{V_0} = \frac{1}{2} \times \left[1 + \text{erf}\left(K \times \frac{y - y_{50}}{x_s}\right)\right] \quad \text{Goertler solution} \tag{8}$$

where $C_2 = -0.0176$, $C_3 = 0.1337$, $C_4 = 0.6876$, V_0 is the free-stream velocity taken as $0.9 \times V_{90}$ as Gonzalez and Chanson [26] and Felder and Chanson [23], $\varphi = y/(a \times x_s)$, $a = (2 \times l_m^2/x_s^2)^{1/3}$, l_m is the Prandtl's mixing length, K is an empirical constant inversely proportional to the shear layer expansion rate, y_{50} is the normal distance from the pseudo-bottom where $V_x = 0.5 \times V_0$, and erf is the Gaussian error function. The results showed strong self-similarity (Fig. 11C) and were consistent with previous studies [26,23,21].

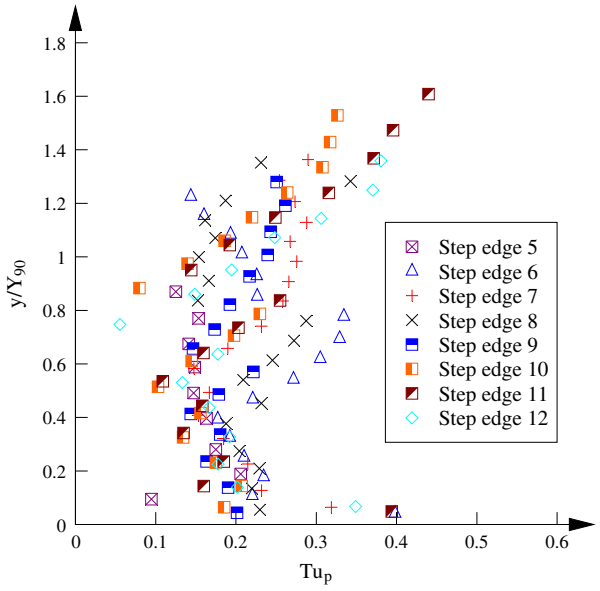

Fig. 9. Turbulence intensity in the water phase of air–water skimming flow – flow conditions: $\theta = 45°$, $h = 0.10$ m, $d_c/h = 0/9$, $Re = 3.3 \times 10^5$, water phase turbulence intensity.

Typical interfacial turbulence intensity distributions above step cavities are shown in Fig. 12. Fig. 12A compares mainstream data, showing significant turbulence levels across the entire water column, typically ranging from 0.4 to 1.0. Local maxima were observed around $y/d_c = 0.3$–0.4, close to the locations of maximum bubble count rates. Next to the pseudo-bottom, the turbulence levels were about 100%, exceeding those documented for mono-phase two-dimensional mixing layers [51]. Large values up to 170% were recorded towards the second half of the step cavity ($x_s/L_{cav} > 0.5$) above the pseudo-bottom. In this region, the overflow reattachment on the horizontal step face led to air bubble fragmentation and strong fluctuations of the interfaces. Fig. 12A includes data on 15.9° and 26.6° stepped chutes [26,23]. The present data was quantitatively consistent with the 26.6° chute, while data in the 15.9° chute were smaller in magnitude. Typical interfacial turbulence intensity contours are plotted in Fig. 12B and C. Overall the data highlighted regions of high interfacial turbulence for $0.3 < y/h < 0.6$, as well as next to the pseudo-bottom. The turbulence levels were larger at step edges than above step cavities, which might be caused by interactions between step edges and large interfacial structures. The turbulence levels were generally independent of the discharge, although higher values were recorded at step edges for the larger discharge possibly because of stronger flow impingement.

7. Discussion

7.1. Relationship between bubble count rate and turbulence intensity

A number of studies observed positive correlations between interfacial turbulence intensity and bubble count rate [17,16,48]. This was also the case during the present study and the data are plotted in Fig. 13 for skimming flows and $(x - x_i)/d_c > 3$. In Fig. 13, present data are compared to an empirical relationship [17]:

$$\text{Tu} = 0.25 + C_1 \times \left(\frac{F \times d_c}{V_c}\right)^p \tag{9}$$

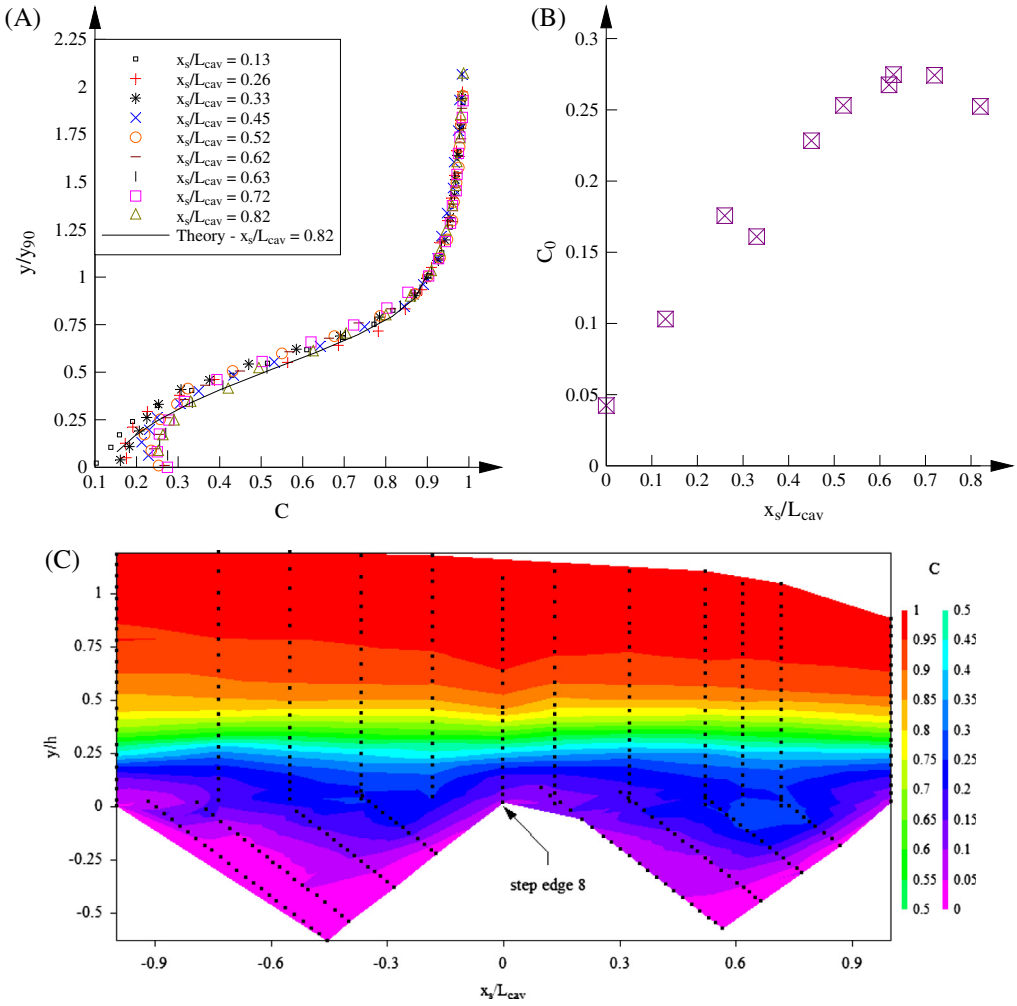

Fig. 10. Void fraction distributions above step cavities in skimming flows – flow conditions: $d_c/h = 0.9$, $Re = 3.3 \times 10^5$, inception point at step edge 5. (A) Void fraction distribution above step cavity, (B) longitudinal variation of void fraction at pseudo-bottom ($y = 0$) and (C) void fraction contours between step edges 7–9 – flow direction from left to right.

where C_1 is a constant of proportionality and p characterises the rate of growth of turbulence intensity with respect to dimensionless bubble count rate, In Eq. (9), Tu = 0.25 for $F = 0$, corresponding to clear water flow measurements upstream of the inception point [34,2]. The best fit of present data yielded $C_1 = 0.24$ and $p = 0.39$ (correlation coefficient $R = 0.78$) and these values are compared to previous data sets in Table 2.

The process of bubble/droplet breakup may be described as a result of turbulent interactions with eddies of similar length scales as the particle [28,31]. Following Kolmogorov [31], a critical Weber number may be used as a simplistic criterion to predict bubble breakup:

$$We_{cr} = \frac{\rho_c \times \overline{v_B^2} \times r_B}{\sigma} \tag{10}$$

where ρ_c is the density of the continuous phase, σ is the air–water surface tension, r_B is the bubble radius, and $\overline{v_B^2}$ is the spatial average value of the square of velocity difference over a distance equalling $2 \times r_B$ in the external flow field [42]. Assuming that the process is ergodic, and $\sqrt{\overline{v_B^2}}$ is the same order as the characteristic interfacial velocity fluctuation $\sqrt{\overline{v^2}}$, the following relationship holds for a constant We_{cr} and a characteristic bubble radius r_B within the inertial subrange:

$$r_B \propto \varepsilon^{-2/5} \tag{11}$$

where ε is the energy dissipation per unit mass and unit time (m^2/s^3):

$$\varepsilon \sim \frac{\overline{v^2}^{3/2}}{L_{int}} = \frac{Tu^3 \times V^3}{L_{int}} \tag{12}$$

since $Tu = \sqrt{\overline{v^2}}/V$, with v the turbulent interfacial velocity fluctuation over the interfacial integral length scale L_{int} measurable by statistical methods [46]. Following Toombes [47], the air–water flow may be reduced to a streamwise distribution of small discrete air and water elements, comprised of the smallest discrete air–water particles of length scale λ, selected such that the probability of one element being air or water becomes independent of its adjacent elements. For a sufficiently large number of bubbles, the bubble count rate may be expressed as:

$$F = \frac{V}{\lambda} \times C \times (1 - C) \tag{13}$$

where V is the interfacial velocity. For a uniform velocity distribution and assuming the smallest length scale λ to be proportional to r_B, it yields:

$$F \propto \frac{Tu^{6/5}}{L_{int}^{2/5}} \times C \times (1 - C) \tag{14}$$

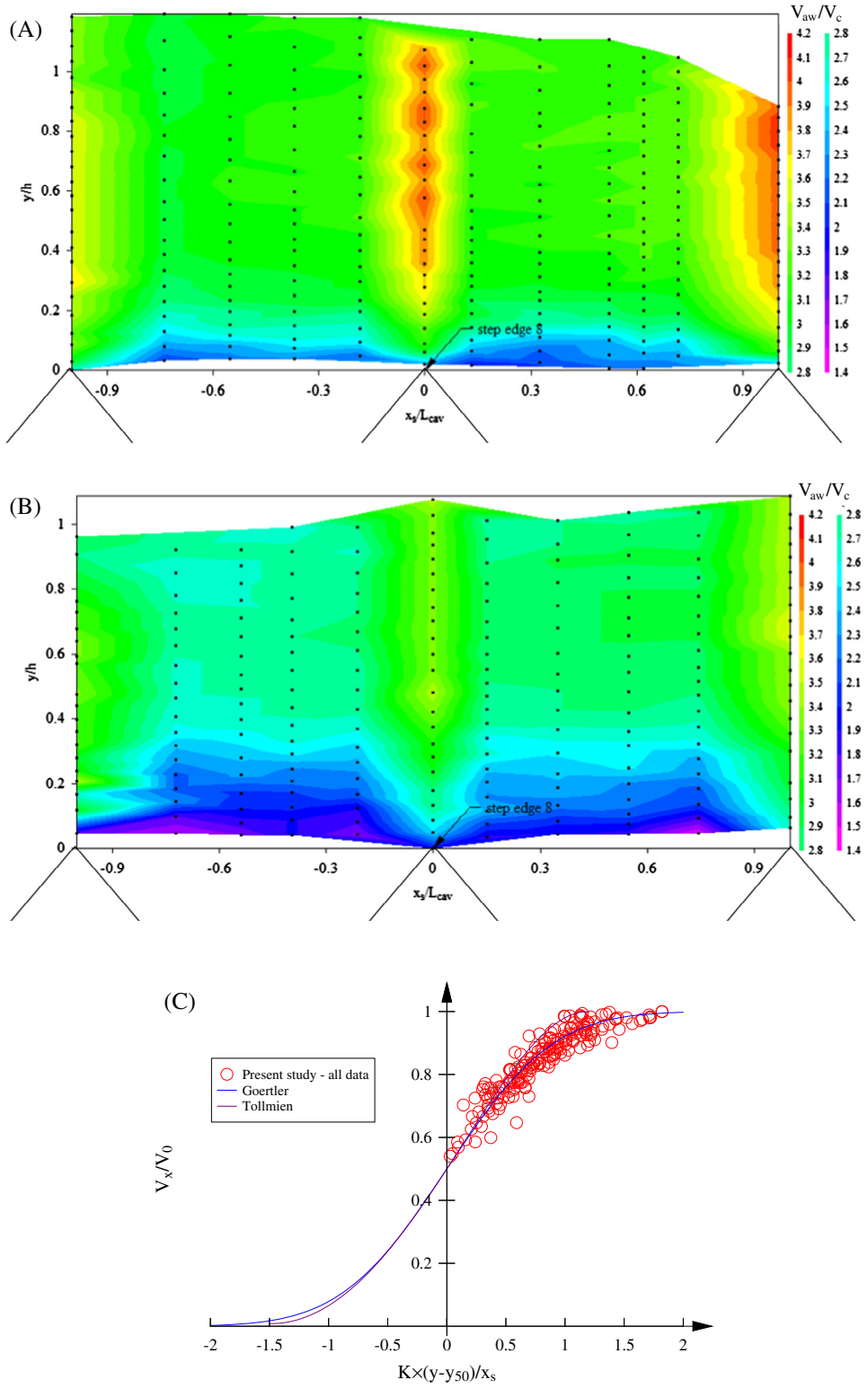

Fig. 11. Interfacial velocity distributions above step cavities in skimming flows. (A) velocity contours between step edges 7–9 – flow conditions: d_c/h = 0.9, inception point at step edge 5, flow direction from left to right, (B) velocity contours between step edges 7–9 – flow conditions: d_c/h = 1.3, inception point at step edge 7, flow direction from left to righ and (C) velocity profiles in the air-water shear layer – flow conditions: h = 0.10 m, d_c/h = 0.9, 1.1, 1.3, 1.5, θ = 45° – comparison with Goertler and Tollmien solutions for developing shear layers.

implying $Tu \propto F^{5/6}/(C \times (1-C))^{5/6}$ if the variation in $L_{int}^{2/5}$ is small across the water column. Eqs. (14) and (9) both suggest a power law relationship between turbulence intensity Tu and bubble count rate F. Eq. (14) shows that Tu vanishes to zero for F = 0, in absence of interface. In contrast, in Eq. (9), the constant offset term (0.25) physically relates to the water phase fluctuations in the clear-water flow immediately upstream of the inception point of free-surface aeration.

Typical experimental data are presented in Fig. 14 for the last step edge. In the legend of Fig. 14, C_{Fmax} denotes the void fraction

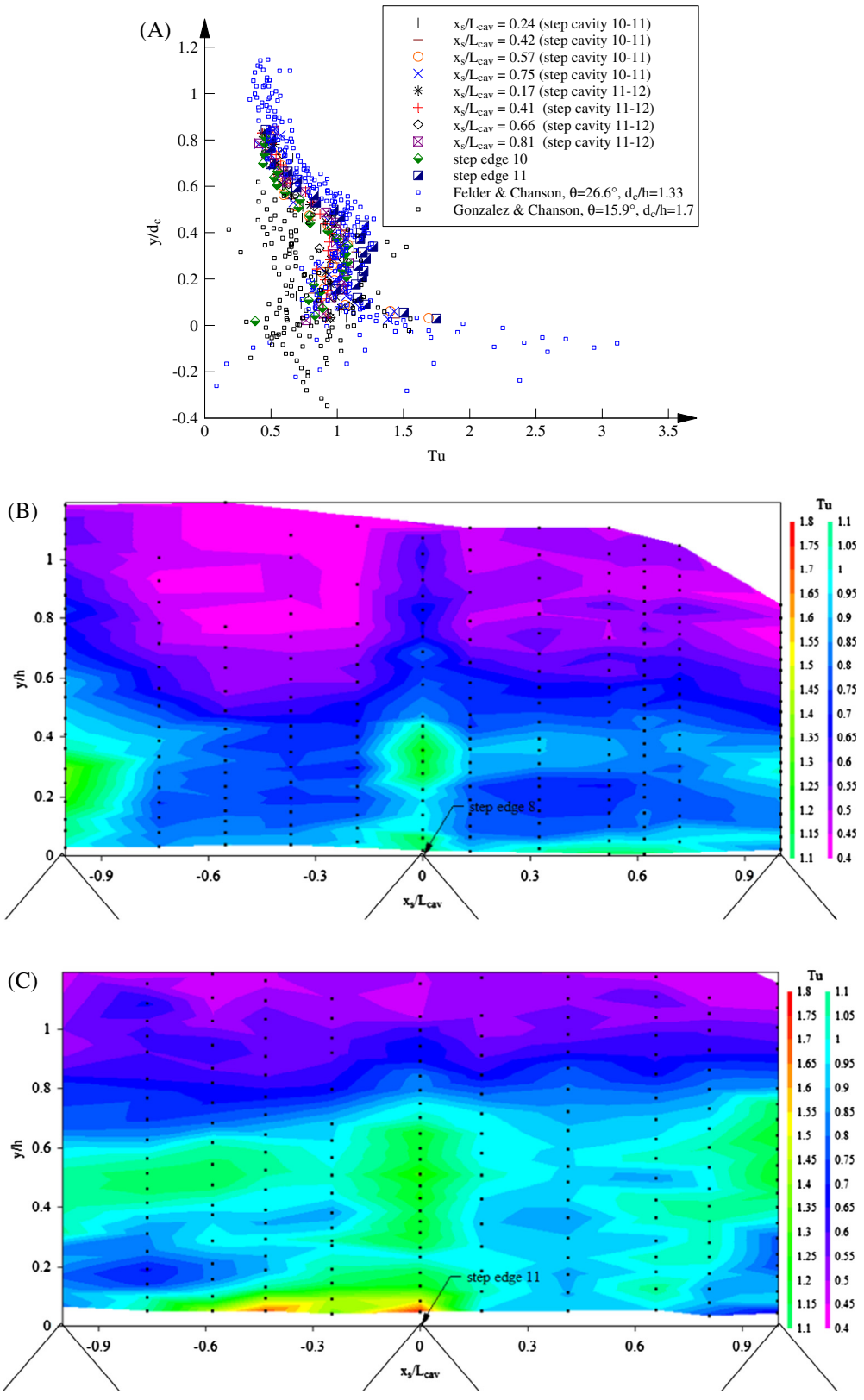

Fig. 12. Turbulence intensity distributions over step cavities in skimming flow. (A) d_c/h = 1.5, inception point at step edge 7 – comparison with data of Gonzalez and Chanson (2004) and Felder and Chanson (2011), (B) turbulence intensity contours above step cavities – flow conditions: d_c/h = 0.9, inception point at step edge 5, flow direction from left to rights and (C) turbulence intensity contours above step cavities – flow conditions: d_c/h = 1.5, inception point at step edge 7, flow direction from left to rights.

where $F = F_{max}$ and the black arrows indicate the direction of increasing elevation above the pseudo-bottom. Typically the data showed two distinct linear trends, marked [1] and [3], plus an intermediate trend marked [2] in Fig. 14. Starting from the pseudo-bottom formed by the step edges, the bubble count rate increased pseudo-linearly with increasing bubble count rate

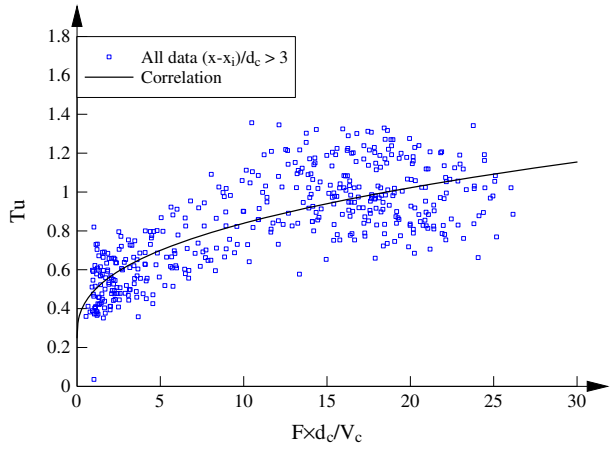

Fig. 13. Relationship between dimensionless bubble count rate $F \times d_c/V_c$ and interfacial turbulence intensity Tu – comparison with Eq. (9).

Table 2
Relationship between interfacial turbulence intensity and bubble count rate in skimming flows on stepped spillways: observed values of C_1 and p (Eq. (9)).

Reference	θ (°)	C_1	p	Remarks
Present study	45.0	0.24	0.39	Flat steps. $Re = 2.3 \times 10^5$–8.8×10^5
Wuthrich and Chanson [50]	26.6	0.55	0.5	Flat steps
		0.25	0.25	Gabion steps
Felder [21]	26.6	0.19	0.54	Flat steps
Toombes and Chanson (2003)	21.8	–	1.5	Flat steps
	15.9			

following the trend [1]. In the mid-air–water column, the bubble count rate reached a pseudo-maximum and remained nearly constant despite increasing turbulence levels, as illustrated by trend [2] in Fig. 14. Trend [3] showed a quasi-linear decrease in bubble count rate with decreasing turbulence up to the upper free-surface. The data showed consistently some form of hysteresis, leading to different slopes between the lower air–water flow region (region [1]) and the upper air–water flow region (region [3]).

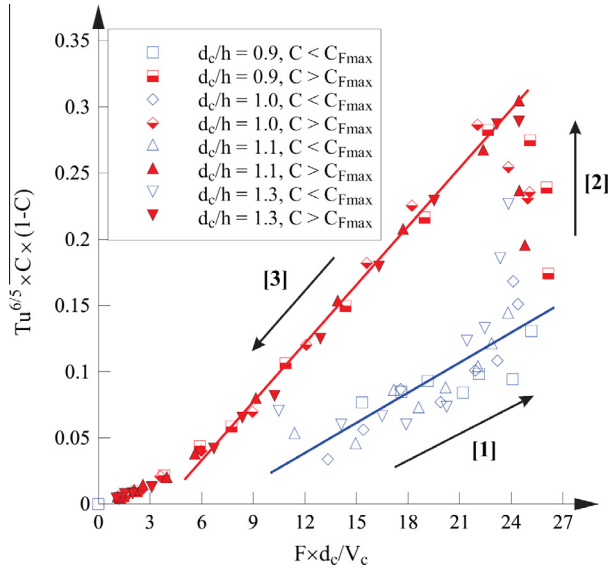

Fig. 14. Dimensionless relationship between bubble count rate and $Tu^{6/5} \times C \times (1 - C)$ in skimming flow: comparison with Eqs. (15a) and (15b) – arrows indicate trend of increasing elevation and increasing time-averaged void fraction – flow conditions: $d_c/h = 0.9$, 1.0, 1.1, 1.3, $\theta = 45°$, step edge 12.

For Fig. 14, the data were best correlated by

$$Tu^{6/5} \times C \times (1 - C) = 0.0076 \times \frac{F \times d_c}{V_c} - 0.052 \quad \text{Region[1]} - C < C_{Fmax} \tag{15a}$$

$$Tu^{6/5} \times C \times (1 - C) = 0.0147 \times \frac{F \times d_c}{V_c} - 0.055$$
$$\text{Region[3]} - C_{Fmax} < C < 0.95 \tag{15b}$$

Both equations are compared to experimental data in Fig. 14, where the different flow rates are indicated in the figure legend.

7.2. Energy dissipation

Based upon the total pressure measurements undertaken along the stepped chute centreline, the time-averaged total head H_t was evaluated as:

$$H_t = \frac{P_t}{\rho_w \times g} + (1 - C) \times z \tag{16}$$

where P_t is the time-averaged total pressure measured by the total pressure sensor, and z is the vertical elevation measured above the spillway toe. The total head H_t is total energy per unit weight of the fluid [27,33]. Dimensionless time-averaged total head distributions are shown in Fig. 15, where y is the distance normal to the pseudo-bottom, d_c is the critical depth, x is the streamwise coordinate with origin at step edge 1, $L_{cav} = 0.141$ m is the step cavity length, and $H_{t,crest}$ is the time-averaged total head above the spillway crest measured relative to the spillway toe. For each discharge, the longitudinal flow pattern was divided into a developing flow region and an aerated flow region. (The location of inception of air entrainment is clearly marked in Fig. 15.) In the developing flow region, the flow was separated into a developing boundary layer and a potential flow region. In the boundary layer, the total head was smallest next to the pseudo-bottom and increased gradually with increasing elevation. The potential flow region showed $H_t/H_{t,crest} \approx 1$, indicating negligible energy loss there. Downstream of the inception point, air was entrained as the boundary layer outer edge extended to the upper free-surface. The total head presented a maximum about $y/d_c = 0.3$, which approximately corresponded to the upper edge of the shear layer. For $y/d_c > 0.3$, the total head decreased rapidly with increasing elevation because of an increasing void fraction.

At each cross-section, the depth averaged total head may be estimated as:

$$H_d = \frac{1}{d} \times \int_0^d H_t \times dy \quad \text{for developing clear water flow} \tag{17a}$$

$$H_d = \frac{\int_0^{Y_{90}} H_t \times dy}{\int_0^{Y_{90}} (1 - C) \times dy} \quad \text{for fully developed air –water flow} \tag{17b}$$

where H_d is the depth averaged total head at a cross-section and d is the clear-water depth. Longitudinal distributions of depth-averaged total head H_d are presented in Fig. 16A. The data trend indicated that the flow energy decreased almost linearly in the downstream direction, for all but the largest discharge ($d_c/h = 1.7$). The finding implied a consistent rate of energy dissipation ($\partial H_d/\partial x$) in both the clear-water and aerated flow regions. For the largest discharge, the rate of energy dissipation over the first few steps was small because the boundary layer was thin compared to the flow depth.

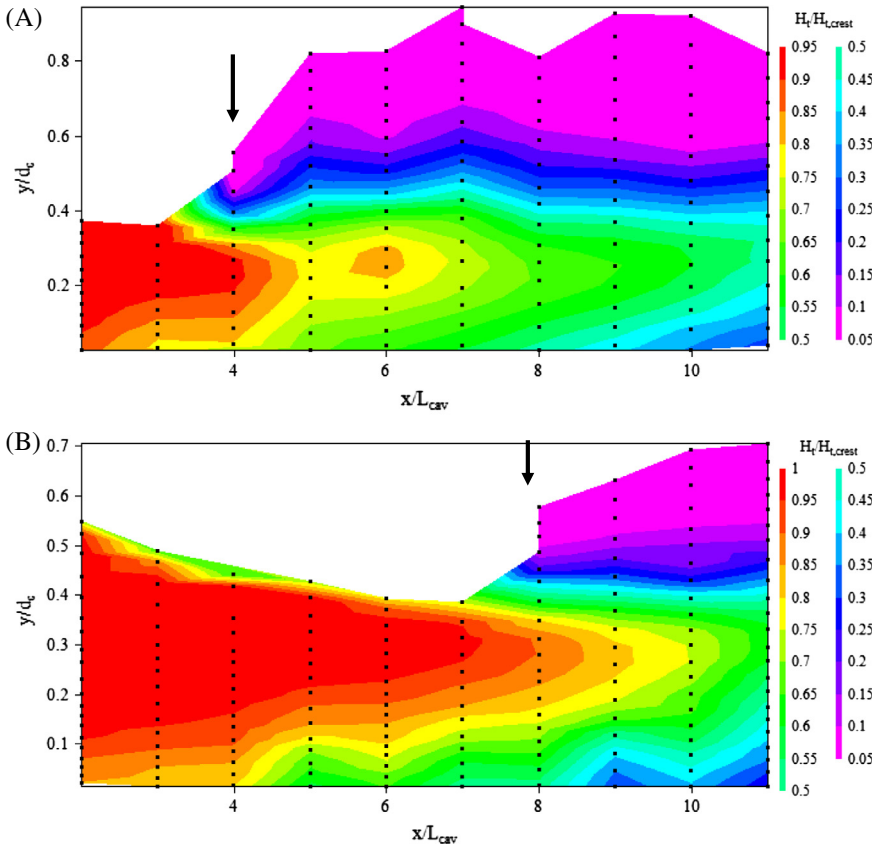

Fig. 15. Dimensionless total head distributions in skimming flows – black dots denote measurement locations and thick black arrow points to the location of inception point of free-surface aeration. (A) $d_c/h = 0.9$, inception point of free-surface aeration at $x/L_{cav} = 4$ and (B) $d_c/h = 1.7$, inception point of free-surface aeration at $x/L_{cav} = 8$.

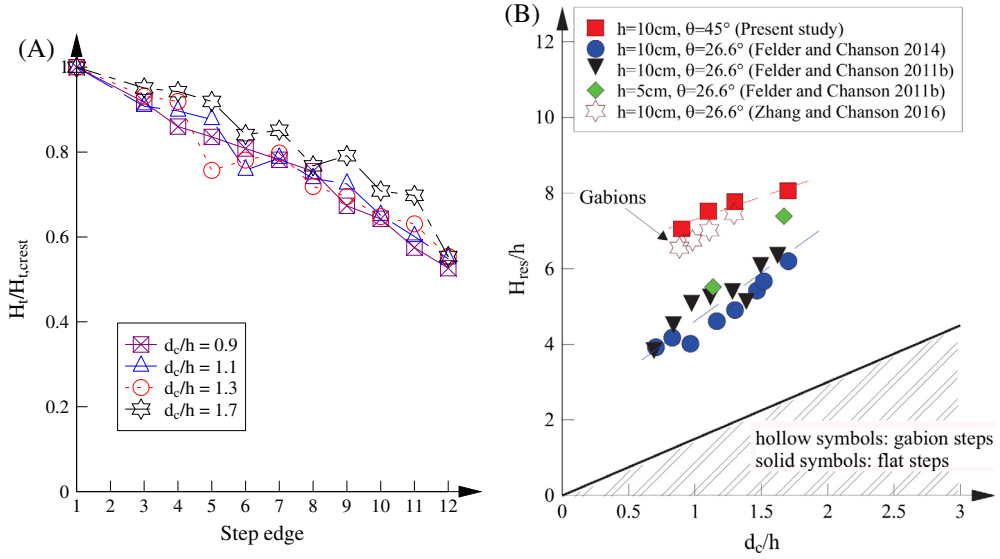

Fig. 16. Energy dissipation along stepped chute. (A) Depth averaged total head along the chute and (B) residual head above the last step edge.

For all discharges, the overall energy dissipation was about 50% at the end of the stepped chute.

Another design parameter is the residual head H_{res}, defined as the depth-averaged total head at the last step edge: i.e., H_d at step edge 12. (Herein both total heads, H_t and H_d, residual head H_{res} and vertical elevation z are measured above the spillway toe.) Residual head data are presented in Fig. 16B. In Fig. 16B, the present data were compared to 26.6° slope data chutes with flat steps [23,24], and a reanalysis of 26.6° gabion stepped chute data [53]. All data corresponded to a very close geometry: namely 1 m and 1.2 m high stepped chutes downstream of a broad-crested weir, and most data were recorded with the same step height: $h = 0.10$ m. Solid symbols correspond to flat impervious steps and hollow symbols to gabion steps in Fig. 16B. For all configurations the dimensionless

residual head H_{res}/h increased with increasing dimensionless discharge d_c/h. For solid (non-gabion) steps, however, the results indicated a marked difference between 45° and 26° slopes:

$$\frac{H_{res}}{h} = 2.05 + 2.6 \times \frac{d_c}{h} \quad 26^\circ \text{ slope with } 0.7 < d_c/h < 1.7 \quad (18a)$$

$$\frac{H_{res}}{h} = 6.1 + 1.19 \times \frac{d_c}{h} \quad 45^\circ \text{ slope with } 0.9 < d_c/h < 1.7 \quad (18b)$$

It is believed that the main difference seen in Fig. 16B was caused by the different cavity aspect ratio, and the chute slope. For completeness, note that the dimensionless residual head has a lower limit, $H_{res}/d_c = 1.5$, corresponding to critical flow conditions [3,27], and shown in Fig. 16B (thick black line).

The large amount of energy dissipation was mostly a result of form loss behind the steps [12,19]. The flow is commonly assumed to be quasi-smooth and its resistance expressed using the Darcy–Weisbach friction factor [39,12]:

$$f_e = 8 \times S_f \times \left(\frac{\int_0^{Y_{90}} (1 - C) \times dy}{d_c} \right)^3$$

for fully-developed air-water flow (19)

where the friction slope S_f is the slope of the total head line: $S_f = -\partial H_d/\partial x$. For each discharge, the friction factor was calculated. In the aerated flow region the friction factors ranged between 0.25 and 0.45. The present data were comparable to previous results [19,14]

Results of the present analyses demonstrated the strong dissipative nature of the stepped chute. The rate of energy dissipation was close between the aerated flow region and the developing flow region, except for the largest discharge where the boundary layer remained thin above the first few step edges (Fig. 16A). The friction factors were high and the rate of energy dissipation was largely determined by the bottom roughness. The stepped bottom induced large form losses in a manner similar to a k-type or d-type rib roughness, the effects of which might be sensitive to the overflow discharge.

8. Conclusion

Detailed air–water flow measurements were conducted in a large facility using both phase-detection and total pressure probes. The stepped chute flow was characterised by strong free-surface aeration and turbulent energy dissipation.

Downstream of the inception point of free-surface aeration, the void fraction distributions presented a S-shape which was modelled by an advection–diffusion equation solution. The location for $C \approx 0.4$–0.5 was characterised by the highest bubble count rate and strongest interfacial turbulence. A theoretical relationship between bubble count rate and interfacial turbulence intensity was derived. In the wake of each step edge, the velocity profiles highlighted an expanding shear layer. The velocity distribution above and inside the shear layer respectively followed respectively a power law and theoretical solutions for a plane shear layer. Simultaneous total pressure and void fraction measurements showed quasi-hydrostatic pressure distributions in the mainstream flow. Energy calculations showed the overall energy dissipation was about 50% regardless of the discharge. The rate of energy dissipation ($\partial H_d/\partial x$) was similar in both the clear-water and aerated flow regions. Overall the data indicated that the bottom roughness (i.e. stepped profile) was the determining factor on the energy dissipation performances of the stepped structure, as well as on the longitudinal changes in air–water flow properties. Further a comparison between present and earlier data suggested that the cavity aspect ratio, hence the slope, has a marked effect on the residual energy.

Acknowledgments

The authors thank Dr Hang Wang (University of Queensland, Australia) for his personal involvement, contribution and comments to the research Project. They acknowledge the technical assistance of Jason Van Der Gevel and Stewart Matthews (The University of Queensland). The financial support through the Australian Research Council (Grant DP120100481) is acknowledged.

References

[1] R. Agostini, A. Bizzarri, M. Masetti, A. Papetti, Flexible Gabion and Reno mattress structures in river and stream training works. Section one: weirs, second ed., Officine Maccaferri, Bologna, Italy, 1987.
[2] A. Amador, M. Sánchez-Juny, J. Dolz, Characterization of the nonaerated flow region in a stepped spillway by PIV, Trans. ASME J. Fluids Eng. 128 (6) (2006) 1266–1273, http://dx.doi.org/10.1115/1.2354529.
[3] B.A. Bakhmeteff, Hydraulics of Open Channels, first ed., McGraw-Hill, New York, USA, 1932. 329 pages.
[4] D.B. Bung, Zur selbstbelüfteten Gerinnenströmung auf Kaskaden mit gemässigter Neigung, (Self-aerated skimming flows on embankment stepped spillways.) Ph.D. thesis, University of Wuppertal, LuFG Wasserwirtschaft and Wasserbau, Germany, 2009, 292 pages (in German).
[5] D.B. Bung, Developing flow in skimming flow regime on embankment stepped spillways, J. Hydraul. Res., IAHR 49 (5) (2011) 639–648, http://dx.doi.org/10.1080/00221686.2011.584372.
[6] D.B. Bung, Non-intrusive detection of air–water surface roughness in self-aerated chute flows, J. Hydraul. Res., IAHR 51 (3) (2013) 322–329. 10.1080/00221686.2013.777373.
[7] G. Carosi, H. Chanson, Turbulence characteristics in skimming flows on stepped spillways, Can. J. Civ. Eng. 35 (9) (2008) 865–880, http://dx.doi.org/10.1139/L08-030.
[8] M.R. Chamani, N. Rajaratnam, Characteristics of skimming flow over stepped spillways, J. Hydraul. Eng., ASCE 125 (4) (1999) 361–368.
[9] H. Chanson, Hydraulics of skimming flows over stepped channels and spillways, J. Hydraul. Res. 32 (3) (1994) 445–460, http://dx.doi.org/10.1080/00221689409498745.
[10] H. Chanson, Hydraulic Design of Stepped Cascades, Channels, Weirs and Spillways, Pergamon, Oxford, UK, 1995. January, 292 pages.
[11] H. Chanson, Historical development of stepped cascades for the dissipation of hydraulic energy, Trans. Newcomen Soc. 71 (2) (2000–2001) 295–318.
[12] H. Chanson, The Hydraulics of Stepped Chutes and Spillways, Balkema, Lisse, The Netherlands, 2001. 418 pages.
[13] H. Chanson, Air–water flow measurements with intrusive phase-detection probes. Can we improve their interpretation?, J Hydraul. Eng., ASCE 128 (3) (2002) 252–255, http://dx.doi.org/10.1061/(ASCE)0733-9429(2002) 128:3 (252).
[14] H. Chanson, Hydraulics of skimming flows on stepped chutes: the effects of inflow conditions?, J Hydraul. Res., IAHR 44 (1) (2006) 51–60, http://dx.doi.org/10.1080/00221686.2006.9521660.
[15] H. Chanson, D. Bung, J. Matos, Stepped spillways and cascades, in: H. Chanson (Ed.), Energy Dissipation in Hydraulic Structures, IAHR Monograph, CRC Press, Taylor & Francis Group, Leiden, The Netherlands, 2015. pp. 45–64.
[16] H. Chanson, G. Carosi, Turbulent time and length scale measurements in high-velocity open channel flows, Exp. Fluids 42 (3) (2007) 385–401, http://dx.doi.org/10.1007/s00348-006-0246-2.
[17] H. Chanson, L. Toombes, Strong interactions between free-surface aeration and turbulence in an open channel flow, Exp. Therm. Fluid Sci. 27 (5) (2003) 525–535, http://dx.doi.org/10.1016/S0894-1777(02)00266-2.
[18] H. Chanson, L. Toombes, Hydraulics of stepped chutes: the transition flow, J. Hydraul. Res., IAHR 42 (1) (2004) 43–54, http://dx.doi.org/10.1080/00221686.2004.9641182.
[19] H. Chanson, Y. Yasuda, I. Ohtsu, Flow resistance in skimming flows and its modelling, Can. J. Civ. Eng. 29 (6) (2002) 809–819, http://dx.doi.org/10.1139/l02-083.
[20] E.J. Ditchey, D.B. Campbell, Roller compacted concrete and stepped spillways, in: H.E. Minor, W.H. Hager (Eds.), Intl Workshop on Hydraulics of Stepped Spillways, Balkema Publ., Zürich, Switzerland, 2000. pp. 171–178.
[21] S. Felder, Air-water flow properties on stepped spillways for embankment dams. Aeration, energy dissipation and turbulence on uniform, non-uniform and pooled stepped chutes, Ph.D. thesis, School of Civil Engineering, The University of Queensland, Brisbane, Australia, 2013.
[22] S. Felder, H. Chanson, Turbulence, dynamic similarity and scale effects in high-velocity free-surface flows above a stepped chute, Exp. Fluids 47 (1) (2009) 1–18, http://dx.doi.org/10.1007/s00348-009-0628-3.

[23] S. Felder, H. Chanson, Air–water flow properties in step cavity down a stepped chute, Int. J. Multiphase Flow 37 (7) (2011) 732–745, http://dx.doi.org/10.1016/j.ijmultiphaseflow.2011.02.009.
[24] S. Felder, H. Chanson, Effects of step pool porosity upon flow aeration and energy dissipation on pooled stepped spillways, J. Hydraul. Eng., ASCE 140 (4) (2014), http://dx.doi.org/10.1061/(ASCE)HY.1943-7900.0000858. 04014002, 11 page.
[25] S. Felder, H. Chanson, Phase-detection probe measurements in high-velocity free-surface flows including a discussion of key sampling parameters, Exp. Therm. Fluid Sci. 61 (2015) 66–78, http://dx.doi.org/10.1016/j.expthermflusci.2014.10.009.
[26] C.A. Gonzalez, H. Chanson, Interactions between cavity flow and main stream skimming flows: an experimental study, Can. J. Civ. Eng. 31 (1) (2004) 33–44, http://dx.doi.org/10.1139/l03-066.
[27] F.M. Henderson, Open Channel Flow, MacMillan Company, New York, USA, 1966.
[28] J.O. Hinze, Fundamentals of the hydrodynamics mechanisms of splitting in dispersion process, J. Am. Inst. Chem. Eng. 1 (3) (1955) 289–295, http://dx.doi.org/10.1002/aic.690010303.
[29] M.W. Horner, An analysis of flow on cascades of steps, Ph.D. Thesis, University of Birmingham, UK, 1969, 357 pages.
[30] S.L. Hunt, K.C. Kadavy, S.R. Abt, D.M. Temple, Impact of converging chute walls for roller compacted concrete stepped spillways, J. Hydraul. Eng., ASCE 134 (7) (2008) 1000–1003, http://dx.doi.org/10.1061/(ASCE)0733-9429(2008) 134:7 (1000).
[31] A.N. Kolmogorov, On the disintegration of drops in a turbulent flow, Doklady Akad. Nauk. SSSR 66 (194H) (1949) 825.
[32] J. Matos, Hydraulic design of stepped spillways over RCC dams, in: Proc. The International Workshop on Hydraulics of Stepped Spillways, Zürich, March 22–24, 2000, pp. 187–194.
[33] J.S. Montes, Hydraulics of Open Channel Flow, ASCE Press, New-York, USA, 1998. 697 pages.
[34] I. Ohtsu, Y. Yasuda, Characteristics of flow conditions on stepped channels, in: Proc. 27th IAHR Biennal Congress, San Francisco, USA, Theme D, 1997, pp. 583–588.
[35] I. Ohtsu, Y. Yasuda, M. Takahashi, Flow characteristics of skimming flows in stepped channels, J. Hydraul. Eng., ASCE 130 (9) (2004) 860–869, http://dx.doi.org/10.1061/(asce)0733-9429(2004) 130:9(860).
[36] L. Peyras, P. Royet, G. Degoutte, Flow and energy dissipation over stepped gabion weirs, J. Hydraul. Eng., ASCE 118 (5) (1992) 707–717, http://dx.doi.org/10.1061/(asce)0733-9429(1992) 118:5(707).
[37] M. Pfister, Effect of Control Section on Stepped Spillway flow, in: Proc. 33rd IAHR Biennial Congress, IAHR–ASCE–EWRI, Vancouver, Canada, 9–14 August, 2009, 8 pages.
[38] N. Rajaratnam, Turbulent jets, Development in Water Science, vol. 5, Elsevier Scientific, New York, N.Y., USA, 1976.
[39] N. Rajaratnam, Skimming flow in stepped spillways, J. Hydraul. Eng., ASCE 116 (4) (1990) 587–591, http://dx.doi.org/10.1061/(asce)0733-9429(1990) 116:4 (587).
[40] J.F. Ruff, K.H. Frizell, Air concentration measurements in highly-turbulent flow on a steeply-sloping chute, Proc. Hydraulic Engineering Conf., ASCE, Buffalo, USA vol. 2 (1994) 999–1003.
[41] H. Schlichting, Boundary Layer Theory, seventh ed., McGraw-Hill, New York, USA, 1979. 329 pages.
[42] M. Sevik, S.H. Park, The splitting of drops and bubbles by turbulent fluid flow, J. Fluids Eng. 95 (1) (1973) 53–60, http://dx.doi.org/10.1115/1.3446958 (8 pages).
[43] R.M. Sorensen, Stepped spillway hydraulic model investigation, J. Hydraul. Eng., ASCE 111 (12) (1985) 1461–1472, http://dx.doi.org/10.1061/(ASCE)0733-9429(1985) 111:12(1461).
[44] M. Takahashi, C.A. Gonzalez, H. Chanson, Self-aeration and turbulence in a stepped channel: influence of cavity surface roughness, Int. J. Multiphase Flow 32 (2006) 1370–1385, http://dx.doi.org/10.1016/j.ijmultiphaseflow.2006.07.001.
[45] M. Takahashi, I. Ohtsu, Aerated flow characteristics of skimming flow over stepped chutes, J. Hydraul. Res. 50 (4) (2012) 427–434, http://dx.doi.org/10.1080/00221686.2012.702859.
[46] H. Tennekes, J.L. Lumley, A First Course in Turbulence, MIT Press, USA, 1972. 300 pages.
[47] L. Toombes, Experimental study of air-water flow properties on low-gradient stepped cascades, Ph.D. Thesis, Dept. of Civil Engineering, University of Queensland, Australia, 2002.
[48] L. Toombes, H. Chanson, Interfacial aeration and bubble count rate distributions in a supercritical flow past a backward-facing step, Int. J. Multiphase Flow 34 (5) (2008) 427–436, http://dx.doi.org/10.1016/j.ijmultiphaseflow.2008.01.005.
[49] H. Wang, F. Murzyn, H. Chanson, Total pressure fluctuations and two-phase flow turbulence in hydraulic jumps, Exp. Fluids 55 (11) (2014), http://dx.doi.org/10.1007/s00348-014-1847-9. Paper 1847, 16 pages.
[50] D. Wuthrich, H. Chanson, Hydraulics, air entrainment and energy dissipation on gabion stepped weir, J. Hydraul. Eng., ASCE 140 (9) (2014), http://dx.doi.org/10.1061/(ASCE)HY.1943-7900.0000919. Paper 04014046, 10 pages.
[51] I. Wygnanski, H.E. Fiedler, The two-dimensional mixing region, J. Fluid Mech. 41 (2) (1970) 327–361, http://dx.doi.org/10.1017/S0022112070000630.
[52] G. Zhang, H. Chanson, H, Hydraulics of the developing flow region of stepped cascades: an Experimental Investigation, Hydraulic Model Report No. CH97/15, School of Civil Engineering, The University of Queensland, Brisbane, Australia, 2015, 76 pages.
[53] G. Zhang, H. Chanson, Gabion stepped spillway: interactions between free-surface, cavity, and seepage flows, J. Hydraul. Eng., ASCE, vol. 142 http://dx.doi.org/10.1061/(ASCE)11 HY.1943-7900.0001120). (In print).